

## CRUSTAL STRESS HETEROGENEITY IN THE VICINITY OF COSO GEOTHERMAL FIELD, CA

Kelly Blake and Nicholas C. Davatzes

Temple University  
1901 North 13<sup>th</sup> Street  
Philadelphia, PA 19128, USA  
e-mail: [tuc17111@temple.edu](mailto:tuc17111@temple.edu) and [davatzes@temple.edu](mailto:davatzes@temple.edu)

### **ABSTRACT**

Borehole induced structures in image logs of wells from the Coso Geothermal Field (CGF), CA record variation in the azimuth of principal stress. Image logs of these structures from five wells were analyzed to quantify the stress heterogeneity for three geologically distinct locations: two wells within the CGF (one in an actively produced volume), two on the margin of the CGF and outside the production area, and a control well several tens of kilometers south of the CGF. Average directions of  $S_{\text{hmin}}$  and its standard deviation are similar along the eastern portion of the geothermal field at  $\sim 106 \pm 28^\circ$ , but this is distinct from the western portion which has an azimuth of  $081 \pm 18^\circ$  and distinct from outside the geothermal field where the average azimuth is  $092 \pm 47^\circ$ . Spectral analysis was applied to the depth variation of stress direction and demonstrates that: (1) the data set contains distinct wavelengths of stress rotation, (2) that the relative power of these wavelengths in the total distribution of stress directions is fractally distributed and (3) in a manner consistent with earthquakes causing the stress rotations. The slope of the power spectrum quantifies the length-scale dependence of stress rotations for the volume of the brittle crust penetrated by each well. While the vertically averaged  $S_{\text{hmin}}$  orientation for the three eastern wells inside the field varied by as little as  $1^\circ$ , the spectral slopes inside the field varied by  $0.4 \log(\text{deg}^2 \cdot \text{m})(\text{m})$ , from the inside to the margin unproduced areas of the CGF.

### **INTRODUCTION**

Local variations in stress are expected to result from topographic relief, crustal buoyancy, transient flow of fluid through rock, temperature gradients, the distribution and geometry of rock masses with different mechanical properties, and fault (earthquake) slip (Zang and Stephansson, 2010). In addition, human activities, such as impoundment of

water behind dams, mine excavation (McGarr et al., 1975), and exploitation of hydrocarbon (e.g., Chan and Zoback, 2007) and geothermal reservoirs (e.g., Segall and Fitzgerald, 1998), have been recognized to change local stress fields (e.g., Barton et al., 1998) and impact earthquake activity (Pearson, 1981; Cornet and Julien, 1989; Fehler, 1989; Jupe et al., 1992). As a practical point, the directions of the principal stresses are highly sensitive to these changes in stress, which act over a range of length-scales, and which can readily be inferred from earthquake data or borehole induced deformation. Variations in stress direction at the tectonic plate scale have been mapped from earthquake and borehole data as part of the world stress map project (e.g., Zoback, 1992). At smaller length-scales stress rotations are commonly visible from the orientation of borehole-induced structures visible in image logs. In geothermal reservoirs the state of stress related to development and maintenance of the geothermal system is of interest for discovering geothermal fields (Davatzes and Hickman, 2006) and for locating wells because of the impact of stress on borehole stability and fracture permeability (e.g., Barton et al., 1995). In enhanced geothermal systems (EGS), heterogeneity in stress is a key control on the potential of fractures to interact with hydraulic stimulation, constrains on the direction the stimulation will grow, and constraints the seismic risk associated with inducing earthquakes on large faults of known orientation.

In this study variation in the orientation of the principal stresses was measured along five wells at a resolution of 0.2 ft for vertical distances up to  $\sim 8000$  ft from borehole-induced deformation visible in image logs along five near-vertical portions of wells in the vicinity of the Coso Geothermal Field (CGF), CA. From the distribution of stress directions with depth in each well, the relative contributions of distinct frequencies of these stress rotations were quantified using spectral analyses. Previously,

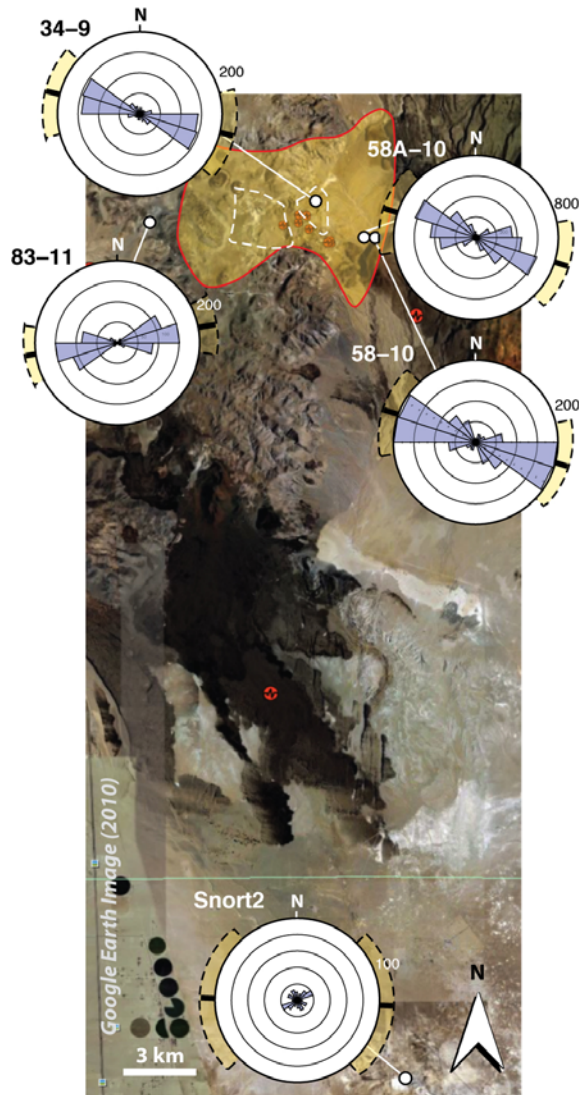


Figure 1: Locations of the five analyzed wells (white circles) in the vicinity of the  $125 \text{ mW/m}^2$  contour of the heat flow anomaly associated with the Coso Geothermal Field (CGF) outlined in red (Duffield and Bacon, 1981).  $S_{\text{hmin}}$  orientations derived from borehole-induced failure are compiled in rose diagrams. In each rose diagram, the thick bar indicates the vertical average whereas the yellow regions indicate  $\pm 1$  standard deviation. Note the smaller white, dashed lines within the heat flow anomaly crudely outline the two main geothermal compartments.

Shamir (1992), Day-Lewis et al. (2010; see also Day-Lewis, 2007), and Valley and Evans (2010) have used this approach. Valley and Evans (2010) note that in the Soultz EGS reservoir stress directions between nearby wells at similar depths can significantly vary. Day-Lewis et al. (2010) proposed

that the stress rotations are primarily controlled by fault slip consistent with large stress rotations predicted from models of fault slip and modeled in boreholes by Shamir (1992) and Brudy and Zoback (1993). Their work showed that the spectral slope of stress rotations is fractal consistent with the early work by Shamir (1992) on short intervals of borehole data and that it mimics the fractal dimension derived from the frequency-magnitude distribution (b-value) of earthquakes. Stress rotation due to fault slip implies large variations in stress direction can be expected over short distances, but also implies that though local principal stress directions vary, the heterogeneity of stress directions can be consistent among nearby wells.

Unlike the previous studies, this study includes multiple wells that span a heavily produced east flank of the CGF (well 34-9RD2DP), unproduced portions of the CGF (well 83-11), the margin of the CGF (wells 58A-10 and 58-10), and outside the geothermal field (SNORT2). Thus from comparisons of these wells, we can test whether the geothermal field has its own distinct stress environment, whether more than 20 years of geothermal production might change these characteristics, and whether the method provides consistent results from two wells that independently sample the same volume.

## GEOLOGIC SETTING OF THE COSO GEOTHERMAL FIELD

The Coso geothermal system is roughly distinguished by the  $125 \text{ mW/m}^2$  heat flow anomaly mapped by Duffield and Bacon (1981) (Figure 1), although continued exploration and analysis of temperature and hydrothermal alteration in wells is refining this boundary. The CGF is further distinguished by high rates of shallow seismicity suggesting a shallowing of the brittle-ductile transition (e.g., Monastero et al., 2005) and extensional strains inferred from focal mechanism inversions (Unruh and Streig, 2002). The produced volumes of the geothermal system are further distinguished by shallow, high temperatures (Kaven et al., 2011, Duffield and Bacon, 1981), low  $V_p/V_s$  ratios (Wu and Lees, 1997; Julian and Foulger, 2011; Kaven et al., 2011), high rates of seismicity with low maximum earthquake magnitude (Unruh and Streig, 2002; Kaven et al., 2011), and volume changes revealed by InSAR (Fialko and Simons, 2000; Wicks et al. 2001). The margin of the geothermal field along Coso Wash is much cooler than the main field and is characterized by low rates of seismicity and low earthquake magnitudes. Outside the geothermal field, seismicity extends to greater depth, and larger earthquake magnitudes occur than in the geothermal system. Although these characteristics distinguish the volumes sampled by

the wells in this study, they all penetrate similar Mesozoic granites and diorites (Adams et al., 2000; Kovac et al., 2005; Manley and Bacon, 2001; Wicks et al., 2001).

### IMAGE LOG ANALYSIS AND STRESS DIRECTIONS

In the first phase of this study GMI Imager was used to map the orientation of the borehole-induced deformation in acoustic and electrical image logs for 34-9RD2DP, 83-11, 58-10, 58A-10, and Snort2. Only vertical portions of wells were mapped to provide the simplest relationship between the principal stresses and borehole deformation assuming an Andersonian stress state and consistent with the stress model developed by Davatzes and Hickman (2006). Tensile Fractures and Breakouts (Figure 2a) which form in response to hoop stresses along the borehole wall (Zoback et al., 2003), and Petal-Centerline Fractures (Figure 2b) which form below the borehole floor during drilling (Davatzes and Hickman, 2010; Gracia-Cruz and Davatzes, 2010) were used to measure the orientation of the horizontal principal stresses using methods summarized in the cited papers. These structures were “picked” in 0.2 ft intervals to trace the local variation in their azimuth. This sampling rate thus define the minimum data spacing, although actual data spacing was often larger due to poor image data or a lack of borehole induced deformation due to stresses insufficient to break the rock along the borehole wall. Identified borehole deformation structures were ranked by the quality of the pick according to the scheme outlined in Davatzes and Hickman (2010) to provide an independent estimate of the reliability of the stress direction. Only induced structures occurring pairs and meeting the criteria summarized in Davatzes and Hickman (2010) were used in this paper.

The vertical average orientation of stress directions interpreted from borehole-induced failure is used to represent the principal stress orientations in a volume similar in scale to the length of the well analyzed (Shamir and Zoback, 1992; Zoback et al., 1989, 2003). This is often taken to represent regional stress directions in locations where the wells penetrate several times deeper than the vertical relief. To first order, it is apparent in Figure 1 and Table 1 that the direction of  $S_{hmin}$  in the three wells within the geothermal field is similar regardless of proximity to production. In addition, the direction of  $S_{hmin}$  is significantly different from two wells outside the geothermal system, although the lack of induced structures in the Snort2 well provides only limited constraints.

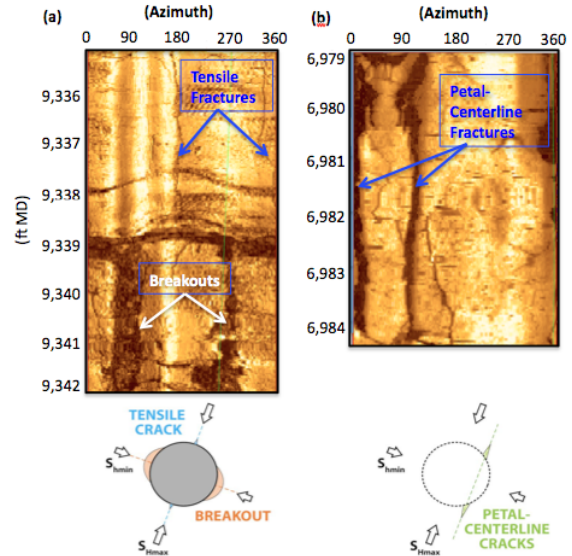


Figure 2: Amplitude image from borehole televiewer log of well 58A-10 shows: (a) Tensile Fractures and Breakouts--inset cartoon demonstrates the relationship of Tensile Fractures and Breakouts to the two horizontal principal stresses; (b) Petal-Centerline Fractures—inset cartoon shows the orientation of Petal-Centerline Fractures to the horizontal principal stresses (Davatzes and Hickman, 2010). All three induced structures were identified in well 58A-10. Only Tensile Fractures and Petal-Centerline Fractures were identified in the other four wells studied.

This standard deviation in  $S_{hmin}$  azimuth for all wells is much larger than the precision of the measurement from individual borehole induced structures. Thus, it must represent a measure of the stress heterogeneity (although one that is insensitive to the wavelength of stress rotations) within the volume sampled by the well. In all cases, inspection of the individual stress directions in the image log reveal that the standard deviation varies from the mean at distinct depths and over distinct wavelengths (Figure 3).

Results from 34-9RD2DP in the east flank production volume and the nearby 58A-10 and 58-10 on the unproduced margin of the geothermal field have indistinguishable  $S_{hmin}$  azimuth and standard deviation (Table 1). There are two ways to characterize this similarity despite difference in production and position within the CGF: (1) the similarity implies decades of production has not measurably altered the regional stress direction or its variability; (2) the similarity is enforced by the proximity of all of these wells to active fault slip on

the Coso Wash fault, which although it has not sustained an historic earthquake offsets holocene alluvial fans (Unruh and Streig, 2002; Davatzes and Hickman, 2006). The distinct orientation  $S_{hmin}$

azimuth and standard deviation measured on the opposite side of the geothermal field in well 83-11 within an unproduced portion of the CGF is consistent with the second alternative (Figure 1).

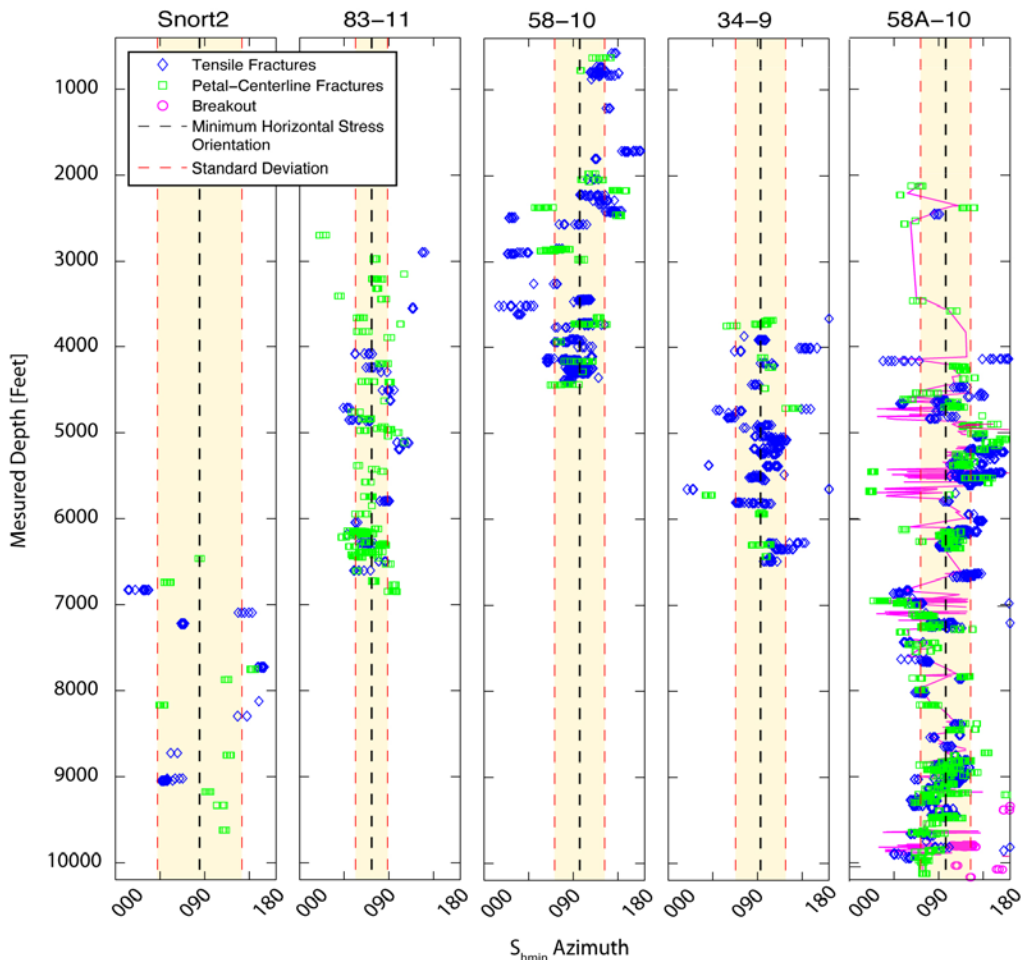


Figure 3:  $S_{hmin}$  azimuth derived from pairs of borehole-induced deformation structures in each of the five wells studied. The uneven sampling of these structures is readily apparent. The vertical average is indicated by the black dashed line and  $\pm 1$  standard deviation is indicated by the yellow region bounded by dashed red lines. The magenta line superimposed on well 58A-10 is the actual waveform used to calculate the power spectrum using the three methods discussed. The line was produced through a linear interpolation of the actual data.

Table 1: Well location and quantified  $S_{hmin}$  orientation for the five studied wells.

Location	Well	$S_{hmin}$ Azimuth
Margin	58A-10	$108 \pm 28^\circ$
Margin	58-10	$107 \pm 28^\circ$
Inside Produced	34-9	$103 \pm 28^\circ$
Inside Unproduced	83-11	$081 \pm 18^\circ$
Outside	SNORT2	$092 \pm 47^\circ$

The well far from the field showed only minor borehole induced deformation, tentatively indicating a vertically averaged  $S_{hmin}$  azimuth of  $092 \pm 47^\circ$ . In this case the large standard deviation in part results in

part from a small data set due to a lack of borehole-induced structures, although large rotations are visible in the data set (Figure 3). The lack of structures implies that insufficient stress was available to overcome the strength of the rock adjacent to the borehole due to small horizontal differential stress and low temperatures that minimize thermal stress.

### SPECTRAL ANALYSIS

The mapped variation in  $S_{hmin}$  (Figure 3) direction varies about the mean to define a relative rotation,

which can be characterized as a superposed series of waveforms with varying wavelength and amplitude. In the analysis we assume that the principal stresses primarily rotate about a vertical axis. This is justified given: (1) studies of induced structures in deviated wells (Peska and Zoback, 1995) have shown that a well must diverge from a principal stress axis by approximately 12-15° to induce significant difference between the azimuth of the principal stress and the azimuth of the induced structure in the image log; this indicates that rotations of the stresses about a horizontal axis less than 12-15° would be practically undetectable; (2) independent evidence for significant differences between the borehole axis and the vertical principal stress such as an echelon tensile fractures were not observed in the intervals studied (Brudy and Zoback, 1993; Peska and Zoback, 1995). With these assumptions, we analyze the dependence of power on the wavelengths of the rotation in stress direction.

A relative measure of how much each wavelength contributes to the aggregate distribution of stress directions is called the power spectral density, which is derived using a Fourier Transform (Hamming, 1989). The relative power of each wavelength defines the spectral slope, which takes the forma of a power law relationship give as:

$$PSD = \lambda^\beta \quad (\text{Equation 1})$$

where PSD is the power spectral density ( $\text{deg}^2 \cdot \text{m}$ ),  $\lambda$  (m) is wavelength, and  $\beta$  ( $\text{deg}^2 \cdot \text{m}$ ) is the power spectral slope.

Sampling of stress directions from borehole deformation provides potentially high resolution but is characterized by irregular sample spacing as well as more extensive gaps between densely sampled intervals resulting from poor data quality or a lack of borehole induced deformation (Figure 3). To define the reliability and uncertainty of the spectral slope impacted by these limitations, sampling characteristics recovered from analysis of the wells at CGF were mimicked in synthetic, power spectra of known fractal slope.

The power spectral slope of the synthetic data set was calculated using the standard periodogram (or single taper) method, the Multitaper method and the Autoregressive Moving Average Spectral Analysis (ARMASA) method. The Multitaper method, implemented as a Matlab toolbox by Thomson (1982) and Percival and Walden (1993) repeatedly analyzes the power spectrum of sub-segments of the data set multiplied by an orthogonal sequence to minimize spectral leakage, and the ARMASA method, also implemented as a Matlab Toolbox (Broersen, 2002,

2009; Broersen et al., 2004), is developed to study irregularly sampled data by generating large numbers of time series models and statistically evaluating their best model. The ARMASA toolbox is available for download and can be obtained at <http://www.dsc.tudelft.nl/Research/Software/index.html>.

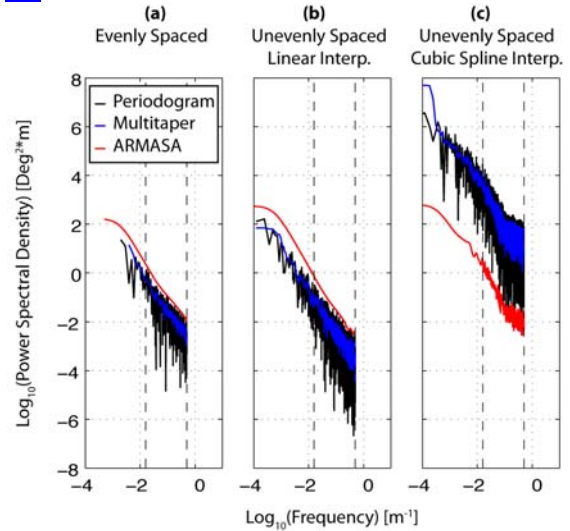


Figure 4: Results of the synthetic fractal data analysis by the three spectral analysis methods applied to the (a) 'best case', where data is continuously sampled at the maximum sample frequency achieved in the well data; and the same synthetic data set but sampled with the distribution of 58A-10 data and then interpolated using (b) linear and (c) cubic-spline algorithm.

Periodogram and multi-taper spectral analyses require constant data spacing across the sampled interval. This requires interpolation of field data to impose regular spacing. To evaluate the effectiveness of the methods in accurately measuring power spectral slope on interpolated data, we analyzed a synthetic dataset constructed from a colored noise generator (Abhirup Lahiri, a matlab function obtainable at [www.mathworks.com](http://www.mathworks.com)) with a known fractal distribution in  $\log_{10}(\text{frequency})$  versus  $\log_{10}(\text{power})$  with power spectral slope of -1.5 ( $\text{deg}^2 \cdot \text{m}$ ) (Figure 4). The actual distribution of data found in each well was used to sample the synthetic distribution of rotations and provide a basis to estimate uncertainty in spectral slope. Both cubic-spline and linear interpolation methods were tested.

From the test of synthetic data, it is apparent that the methods produce similar slopes in the data set sampled at an even spacing of 0.2 ft. This case corresponds to the best case possible in the image log analysis (Figure 4a) and summarized in Table 2.

Once the synthetic data is sampled corresponding to the distribution of data in well 58A-10 and then linearly interpolated the resulting power spectral slope increases, suggesting more power is being attributed to the longer wavelengths at the expense of shorter wavelengths as expected (Figure 4b). This interpolation is illustrated in Figure 3. However, all methods recover the spectral slope within  $+0.2 \text{ deg}^2 \cdot \text{m}$ , and find fractal distributions in power. Cubic-spline interpolation results in a minor break in slope at a frequency of approximately  $\sim 0.1 \text{ m}^{-1}$  (Figure 4c). At short frequencies, the power spectral slope is over-estimated by  $\sim 2x$ , whereas at higher frequencies spectral slope is slightly underestimated. We also note that the actual power recovered depends on the method applied.

This test was repeated for the linearly interpolated data distribution in each well to estimate the uncertainty of each method in that case. The results are summarized in Table 2 and spectral slopes were chosen for comparison from the method with the least modeled uncertainty. Note that a single method does not appear to consistently minimize this estimate of uncertainty and is a subject of continued investigation (Table 2).

The power spectral methods used assume a function is periodic and stationary, or in other words that power is associated with wavelengths that do not depend on position in the data series (i.e., depth). Similarly, a fractal distribution should show the same scaling of power with frequencies at all length-scales. We tested for these characteristics by comparing subsections containing high sample density and continuity of data from extreme portions of the data series in well 58A-10 (Figure 5). They show power spectral slopes given by Multitaper (blue) and ARMASA (red) are different than the overall distribution and with regard to each other. The greatest difference is a shallow depth and are minimized in the deepest interval. Differences in spectral slope that depend on depth could indicate a change in mechanism controlling stress heterogeneity or dependence of properties like shear stress drop on depth. We note however that the power spectral slope is derived from a relatively short data window, which makes the linear regression for the slope less certain. Inspection of the power spectra derived from whole well analysis (Figure 6) does indicate linear distributions.

The two wells on the same well pad, 58A-10 and 58-10, which are much taller than their horizontal separation, provide two independent measures of the stress heterogeneity in the same volume. Comparing these wells reveals that each is characterized by

distinct  $S_{\text{hmin}}$  directions at similar depths (Figure 3). However, the power spectral slope indicates they experience the same stress heterogeneity consistent with our hypothesis (Figure 6 and Table 2). Well 34-9RD2DP, within a produced area of the CGF, has a spectral slope that is different from the 58A-10 and 58-10 wells by  $>0.4 \text{ (deg}^2 \cdot \text{m)}$ , in excess of the estimated uncertainty (Figure 6).

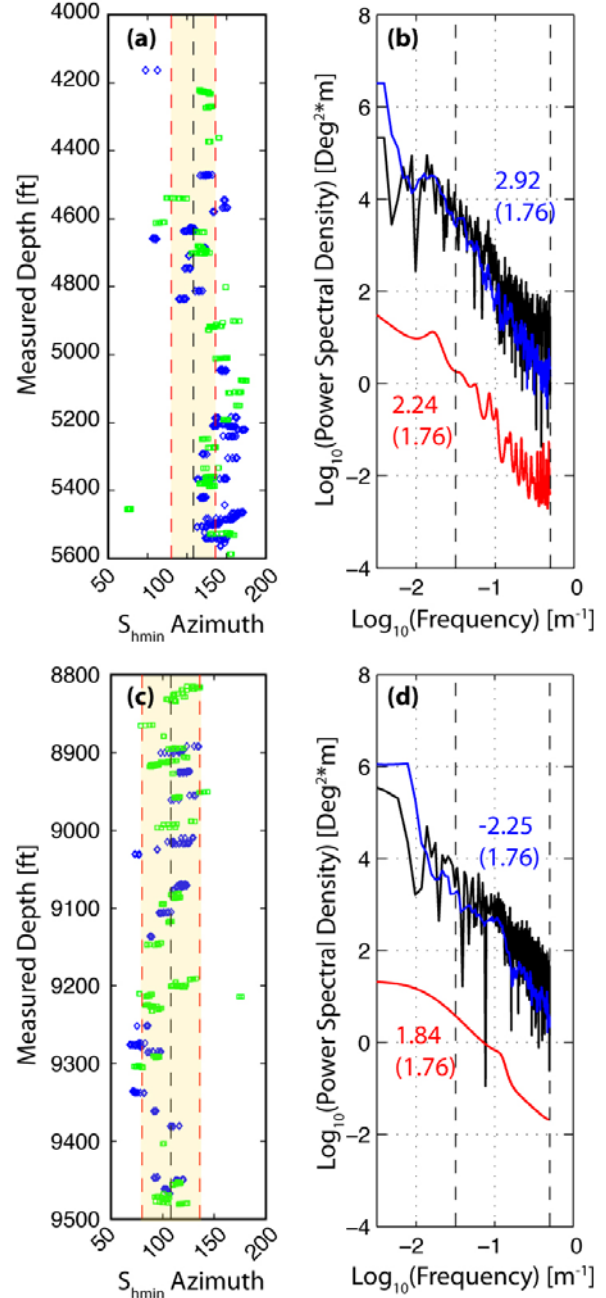


Figure 5: Power spectra of sub-regions of high data density sampled from well 58A-10. (a) Shallowest interval of “continuously” sampled data and (b) corresponding power spectrum. (c) Deepest interval of “continuously” sampled data and (d) corresponding power spectrum.

Thus, unlike the analysis of the average  $S_{hmin}$  azimuth and standard deviation, the power spectral slopes imply that the stress heterogeneity inside the produced geothermal field is distinct from the margin of the geothermal field. The similar standard deviation of  $S_{hmin}$  azimuth, but different spectral slope implies there is the same amount of heterogeneity, but that its distribution among wavelengths are different. The shallower slope is in 58A-10 and 58-10 are actually consistent with the relatively low rate of seismicity and earthquake magnitudes in Coso Wash as compared to the production zone containing 34-9RD2DP (Davatzes et al., 2006; Kaven et al., 2011). Within the CGF, power spectral slopes are similar regardless of production history or proximity to the Coso Wash Fault.

The average  $S_{hmin}$  azimuth and standard deviation indicated by SNORT2 outside the CGF are distinct from inside the CGF, which implies a distinct tectonic environment dominates the geothermal system. The best test of this tectonic sub-environment would be provided by a more distant well such as SNORT2. However we note that power spectral slopes reported for SNORT2 in Table 2 results from a small data set, and are assigned apparently low uncertainties. However it is clear that such a small number of observations constraining the power spectrum makes it easily biased and on this basis we choose not to compare its spectral slope to those within the field.

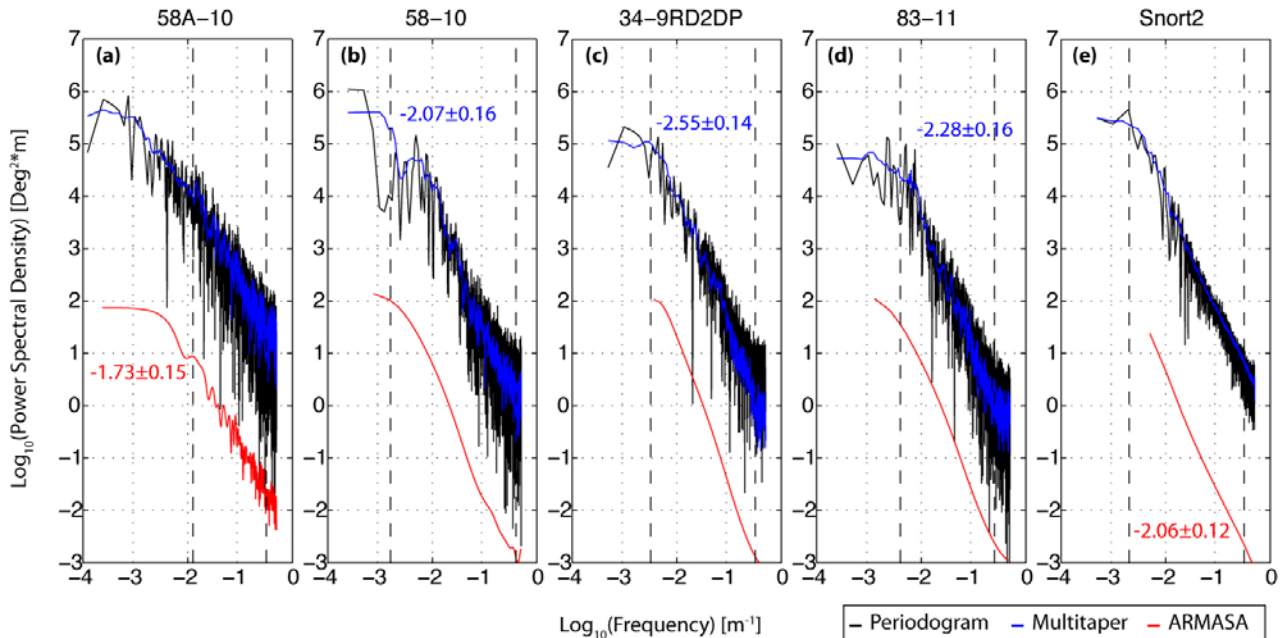


Figure 6: Power spectra derived for each of the wells. The inset table summarizes the slopes using the method associated with least uncertainty.

**Table 2:** Wells with calculated spectral slopes,  $\log_{10}(\text{degree}^2 \cdot \text{m})$ , obtained from linearly interpolated stress direction data.

Well	Periodogram	Multitaper	ARMAS	Frequency Range
Best Case (Synthetic)	-1.49±0.01	-1.47±0.03	<b>-1.50±0.00</b>	N/A
58A-10 (Margin)	-1.75±0.19	-1.76±0.22	<b>-1.73±0.15</b>	0.0033-0.40 (303.3-2.5)
58-10 (Margin)	-2.04±1.25	<b>-2.07±0.16</b>	-2.19±0.22	0.0015-0.22 (666.6-4.5)
34-9RD2DP (Inside Produced)	-1.97±0.14	<b>-2.55±0.14</b>	-2.64±0.14	0.0037-0.31 (270.3-3.2)
83-11 (Inside Unprod.)	-2.12±0.22	<b>-2.28±0.16</b>	-2.24±0.18	0.00040-0.28 (250-3.57)
SNORT2 (Outside)	-2.06±0.17	-1.96±0.2	<b>-2.06±0.12</b>	0.0020-0.30 (500-3.2)

## DISCUSSION

The elastic strain energy stored in a rock due to the applied principal stresses can be released by breaking bonds in fracture formation and or through fault slip (Sholz, 1990). In the case of fracture slip, this release of strain energy produces an earthquake that preferentially expends shear stress, causing local rotations of principal stress directions. Similarly, the displacements associated with fracture propagation produces a change in the principal stress orientation on that fault and is transferred into elastic energy at the fault tip (Sholz, 1990). In either case this release of elastic energy must correlate to a change in the principal stress direction and the magnitude of an earthquake (Sholz, 1990). Injection and extraction modulation of fluid pressure cause changes in effective normal stress which can cause slip on existing faults or the creation of new faults producing earthquakes (Pearson, 1981; Cornet and Julien, 1989; Fehler, 1989; Jupe et al., 1992) or changes in solid stresses accompanying volume changes to similar effect. The ubiquitous and heterogeneous stress rotations in the five wells, therefore, could be the result of fault (earthquake) slip.

Following Day Lewis (2007) and Day-Lewis et al. (2010), the Gutenberg-Richter Law defines the relationship between earthquake magnitude and its frequency as:

$$\log N = a - bM \quad (\text{Equation 2})$$

where N is the number of earthquakes, M is the earthquake magnitude, a is the y-axis intercept and b is the slope of the frequency-magnitude relationship. Earthquake b value for the Coso Range is 2.4 and for Indian Wells is 2.1 (Glazner et al. 2002) using data from the Southern California Earthquake Network.

The correlation between stress rotations and earthquakes is demonstrated by the earthquake fractal dimension:

$$D_{eq} = \frac{bd}{q} \quad (\text{Equation 3})$$

where d and q are constants and  $D_{eq}$  is the earthquake fractal dimension that represents the relationship between moment magnitude and fault surface area with units of  $\log(10^{27} \text{ dyne*cm})/\log(10^3 \text{ km}^2)$  (Day-Lewis, 2007). Both  $D_{eq}$  and spectral slope scale to fault size, and thus can be compared to discover a correlation between local heterogeneity in principal stress directions and earthquake frequency-magnitude in the vicinity of Coso.

Using constants 1.5 for q corresponding to a circular

fault and a range of 2 to 3 for d which represents the amount of stress drop that occurred during fault slip (Day-Lewis, 2007, Kanamori and Anderson, 1975 and Wesnousky et al., 1983). Note using these as constants is an ad hoc assumption that implies that shear stress drop is independent of depth or fault dimensions. Thus, the earthquake fractal dimension calculated from these constants and the b-value for the Coso Range, which includes all portions of the geothermal field, ranges from 3.2-4.8. For Indian Wells, which includes the location of SNORT2, the fractal dimension is 2.8-4.2.

The fractal dimension of stress rotation,  $D_{rot}$ , is derived from the power spectral slope,  $\beta$ , using:

$$D_{rot} = \frac{5 - \beta}{2} \quad (\text{Equation 4})$$

This equation gives the results in Table 3, which suggests that the fractal dimensions of these two phenomena are consistent which suggests that seismicity can account for the heterogeneity in stress direction.

**Table 3: Comparison of Fractal Dimensions**

Well	$\beta$	$D_{rot}$	$D_{eq}$
58A-10	-1.73±0.15	3.37	3.2-4.8
58-10	-2.07±0.16	3.54	
34-9RD2	-2.55±0.14	3.78	
83-11	-2.28±0.16	3.64	
SNORT2	-2.06±0.12	3.53	2.8-4.2

More detailed evaluation of the control of seismicity on stress heterogeneity could be tested using the seismicity detected by the local Coso Seismic Network, which has a low detection threshold, and with re-locations to focus examination onto the small volume in the vicinity of the well. To date, such a comparison has not been conducted. Similar changes in micro-seismicity have been observed in other locations in the presence of normal production-injection activity such as the Geysers (Majer and Peterson, 2007) and during EGS stimulation (e.g., Soutz, Concha et al., 2010 and Evans et al. 2005).

Two of the studied wells are from the same well pad, have similar deviation and are analyzed across overlapping depths. For these wells, the depth and wavelength of the specific stress rotations commonly differ. However, as noted the standard deviation and power spectral slopes are similar. This contrast implies the same heterogeneity of stress direction in the volume is measured by both wells despite differences at specific depths related to individual rotations. If fault slip is responsible for stress rotations, stress directions should diverge in very closely spaced wells as observed, due to the position

of the well and the relative position of individual faults. Since the slope of the power spectrum is similar, this implies similar populations of slipped faults contribute to stress rotation in each well.

## CONCLUSIONS

The  $S_{\text{hmin}}$  orientations for five wells within the vicinity of CGF were calculated by observing induced structures to be  $108\pm 28^\circ$  and  $107\pm 28^\circ$  on the eastern margin of the geothermal field,  $103\pm 28^\circ$  one of the eastern production volumes of the CGF, and inside the unproduced CGF on the west side is  $081\pm 18^\circ$ . These variations are consistent with relative small impacts of product on the average  $S_{\text{hmin}}$  azimuth and stress heterogeneity relative the potential role of the Coso Wash Fault in controlling stress in the eastern portion of the CGF. Outside the geothermal field in Indian Wells, a sparse data set in SNORT2 indicates  $S_{\text{hmin}}$  is oriented  $092\pm 47^\circ$ , but nevertheless suggesting that there is a variation in the principal stress directions between these two regions.

The fractal dimension derived from the power spectral slopes calculated using spectral analysis methods Periodogram, Multitaper and ARMASA in the unproduced region of the geothermal are consistent with the fractal dimensions derived from b-values in corresponding regions. This correspondence circumstantially suggests that seismicity plays a critical role in controlling stress heterogeneity in and around the Cosos Geothermal Field.

## ACKNOWLEDGEMENTS

We would like to acknowledge Steve Bjornstad of the Navy Geothermal Office and Jess McCoullough of Terra-gen Power for generously providing the Coso Geothermal Field image log data used in this study. This research also benefited from scientific correspondence with Amy Day-Lewis, Steve Hickman, Olé Kaven Stijn de Waele and Piet Broersen. Funding for this project is through Temple University.

## REFERENCES

Adams, M.C., Moore, J.N., Bjornstad, S., and Norman, D.I. (2000), Geologic history of the Coso geothermal field. *Proceedings World Geothermal Congress 2000, Kyushu – Tohoku, Japan, May 28 – June 10, 2000*. p. 2463-2469.

Broersen, P.M.T. (2002), Automatic Spectral Analysis with Time Series Models, *IEEE Transactions on Instrumentation and Measurement*, v. 51, p. 211-216.

Broersen, P.M.T. (2009), Practical Aspects of the Spectral Analysis of Irregularly Sampled Data with Time-Series Models, *IEEE Transactions on Instrumentation and Measurement*, v. 58, p. 1380-1388.

Brudy, M. and Zoback, M.D. (1993), Compressive and tensile failure of boreholes arbitrarily-inclined to principal stress axes: Application to the KTB boreholes, Germany, *International Journal of Rock Mechanics and Mining Sciences*, v. 30, p. 191-215.

Chan, Alvin W. and Zoback, M.D. (2007), The role of hydrocarbon production on land subsidence and fault reactivation in the Louisiana Coastal Zone, *Journal of Coastal Research*, v. 23, p. 771-786.

Cornet, F.H. and Julien, P. (1989), Stress determination from hydraulic test data and from mechanisms of induced seismicity, *Int. J. Rock Mech. Min. Sci. Geomech. Abstr.* v. 26 (3/4), p. 235– 248.

Davatzes, N.C., and Hickman, S. (2006), Stress and faulting in the Coso Geothermal Field: Update and recent results from the East Flank and Coso Wash, *Proceedings 31<sup>st</sup> Workshop on Geothermal Reservoir Engineering*, Stanford Univ., Stanford, CA, SGP-TR-179.

Davatzes, N. C and Hickman, S. (2010), The feedback between stress, faulting, and fluid flow: Lessons from the Coso Geothermal Field, CA, USA. *Proceedings World Geothermal Congress 2010*. p. 1-14.

Day-Lewis, A. (2007), Characterization and Modeling of In Situ Stress Heterogeneity, Ph.D. Thesis, Stanford University, 121 p.

Day-Lewis, A., Zoback, M.D. and Hickman, S. (2010), Scale-invariant stress orientations and seismicity rates near the San Andreas Fault, *Geophys. Res. Lett.*, 37, L24304, doi:10.1029/2010GL045025.

Duffield, W.A., Bacon, C.R. and Dalrymple, G.B. (1980), Late Cenozoic volcanism, geochronology, and structure of the Coso Range, Inyo County, California. *J. of Geophys. Research*, v. 85, p. 2381-2404.

Fehler, M.C. (1989), Stress control of seismicity patterns observed during hydraulic fracturing experiments at the Fenton Hill Hot Dry Rock Geothermal Energy Site, New Mexico. *Int. J. Rock Mech. Min. Sci. Geomech. Abstr.* v.26 (3/4), p. 211–219.

- Fialko, Yuri, & Mark Simons. (2000), Deformation and seismicity in the Coso Geothermal area, Inyo County, California: Observations and modeling using satellite radar interferometry, *J. of Geophys. Research*, v. 105, p. 781-21,794.
- Glazner, A.F., Walker, J.D. and Bartley, J.M. (2002), Mojave Desert and Southern Basin and Range, Geological Society of America, Boulder, CO.
- Gutenberg, B., and C.F. Richter. (1944), Frequency of earthquakes in California: *Bulletin Seismology Society of America*, v. 34, p. 185-188.
- Hamming, R.W. (1989), Digital Filters: Third Edition. Dover Publications, Inc., Mineola, 284.
- Jupe, A.J., Green, A.S.P. and Wallroth, T. (1992), Induced microseismicity and reservoir growth at the Fja  $\square$ llbacka hot dry rocks project, Sweden. *Int. J. Rock Mech. Min. Sci. Geomech. Abstr.* v. 29 (4), p. 343–354.
- Kanamori, H., and Anderson, D.L. (1975), Theoretical basis of some empirical relations in seismology, *Bull. Seismol. Soc. Am.*, v. 65, p. 1073-1095.
- Kaven, J.O., Hickman, S., and Davatzes, N.C. (2011), Microseismicity, fault structure and hydraulic compartmentalization within the Coso Geothermal Field, California, Proceedings, Thirty-Sixth Workshop on Geothermal Reservoir Engineering, January 31-February 2, 2011, 10 p.
- Kovac, K.M., Moore, J.N., and Lutz, S.J. (2005) Geological framework of the East Flank, Coso geothermal field: Implications for EGS development. *Proceedings 30<sup>th</sup> Workshop on Geothermal Reservoir Engineering, Stanford, CA, Jan31-Feb2. SGP-TR-176*, 7 p.
- Majer, E. L., and Peterson, J.E., (2007), The impact of injection on seismicity at The Geysers, California Geothermal Field: *International Journal of Rock Mechanics and Mining Sciences*, v. 44, p. 1079-1090.
- Manley, C.R. and Bacon, C.R.. (2000), Rhyolite thermobarometry and the shallowing of the magma reservoir, Coso Volcanic Field, California, *Journal of Petrology*, v. 41, p. 149-174.
- McGarr, A., Spottiswoode, S.M., and Gay, N.C. (1975), Relationship of Mine Tremors to Induced stresses and to rock properties in the focal region. *Bulletin of the Seismological Society of America*, v. 65, p. 981-993.
- Monastero, F.C., Katzenstein, A.M., Miller, S.J., Unruh, J.R., Adams, M.C. and Richards-Dinger, K. (2005), The Coso geothermal field: A nascent metamorphic core complex. *GSA Bull.*, **117**(11/12), 1534-1553.
- Pearson, C. (1981). The relationship between microseismicity and high pore pressures during hydraulic stimulation experiments in low permeability granitic rocks, *J. Geophys. Res.* v. 86 (B9), p. 7855–7864.
- Percival, D.B., and Walden, A.T. (1993), *Spectral Analysis for Physical Applications: Multitaper and Conventional Univariate Techniques*, Cambridge University Press.
- Peska, P. and Zoback, M.D. (1995), Compressive and tensile failure of inclined wellbores and determination of in situ stress and rock strength, *J. of Geophys. Research.* v. 100, p. 12791-12811.
- Segall, P. and Fitzgerald, S.D. (1998), A note on induced stress changes in hydrocarbon and geothermal reservoirs, *Tectonophysics*, v. 289, p. 117-128.
- Shamir, G., and Zoback, M.D. (1992), Stress orientation profile to 3.5 km depth near the San Andreas fault at Cajon Pass, California, *J. of Geophys. Research*, v. 97, p. 5059-5080.
- Scholz, 1990
- Thomson, D.J. (1982), Spectrum estimation and harmonic analysis, *Proceedings of the IEEE*, v. 10. p. 368-370.
- Unruh, J.R., and Streig, A.R. (2004), Mapping and characterization of neotectonic structures in a releasing stepover, northern Coso Range, eastern California, *Final technical report submitted to the U.S. Navy Geothermal Program Office, China Lake Naval Air Warfare Center, Contract N68936-02-C-0208*, p. 46
- Unruh, J.R., and Streig, A.R. (2004), Mapping and characterization of neotectonic structures in a releasing stepover, northern Coso Range, eastern California: Final technical report submitted to the U.S. Navy Geothermal Program Office, China Lake Naval Air Warfare Center, Contract N68936-02-C-0208, 46 p.
- Valley, B and Evans, K.F. (2010), Stress Heterogeneity in the Granite of the Soultz EGS Reservoir Inferred from Analysis of Wellbore Failure, *Proceedings World Geothermal Congress 2010*, Bali, Indonesia.
- Wesnousky, S.G., Scholz, C.H., Shimazaki, K. and Matsuda, T. (1983), Earthquake frequency distribution and the mechanics of fault, *J. of Geophys. Research*, v. 88, p. 9331-9340.

- Wicks, C.W., Thatcher, W., Monastero, F.C. and Hasting, M.A. (2001), Steady-state deformation of the Coso Range, east-central California, inferred from satellite radar interferometry, *J. of Geophys. Research*, v. 106, p. 13,769-13,780.
- Zang, A. and Stephansson, O. (2010), Stress Field of the Earth's Crust, Springer, Dordrecht, 322 p.
- Zoback, M.L. (1992), First and second order patterns of stress in the lithosphere: the World Stress Map project. *J. of Geophys. Research* v. 97, p. 11703-11728.